

# The Steepness Ratio Technique: A New Method to analyze ROSAT All-Sky Survey Extended Sources

S. De Grandi<sup>1,2</sup>, S. Molendi<sup>3</sup>, H. Böhringer<sup>1</sup>,  
G. Chincarini<sup>2,4</sup> and W. Voges<sup>1</sup>

## ABSTRACT

In this first paper of a series we develop a new technique to analyze clusters of galaxies observed during the ROSAT All-Sky Survey (RASS). We call this method the Steepness Ratio Technique (SRT). The SRT uses the convolution between the real RASS point-spread function and the cluster emission profile assumed to be a  $\beta$ -model with the  $\beta$  parameter fixed to the value of 2/3. From the convolved source emission profile the SRT extracts total flux and extension (i.e., core radius) for each cluster. Using the Steepness Ratio (SR) and a control sample of RASS pointlike sources we are able to assign to each RASS source a model-independent probability of extension. Potential biases arising from the hypotheses of a  $\beta$ -model emission profile and from a fixed  $\beta$  value are quantified. Tests with control samples of optically identified sources extracted from both the ROSAT survey database and from the ROSAT-PSPC pointed observations archive are performed to check the SRT output. We find that the source properties derived using the SRT on RASS data are consistent with those determined from ROSAT-PSPC pointed observations.

*Subject headings:* methods: data analysis — X-rays: clusters of galaxies

---

<sup>1</sup>Max-Planck-Institut für extraterrestrische Physik, Giessenbachstrasse 1, D-85740 Garching, Germany

<sup>2</sup>Università di Milano, via Celoria 16, I-20100 Milano, Italy

<sup>3</sup>Istituto di Fisica Cosmica, CNR, via Bassini 15, I-20133 Milano, Italy

<sup>4</sup>Osservatorio Astronomico di Brera, via Brera 28, I-20121 Milano, Italy

## 1. Introduction

The first part of the ROSAT mission (Trümper 1993) was dedicated to the All-Sky Survey (RASS; Voges 1992), carried out with the Position Sensitive Proportional Counter (PSPC; Briel & Pfeiffermann 1986) as focal plane detector. Given the vast area explored during the ROSAT survey, in practice the whole sky, the RASS data provide a unique opportunity to construct a large sample of X-ray sources, that can be used for detailed cosmological and statistical studies. This is exploited in the frame of the ESO Key Program Redshift Survey of southern sky clusters of galaxies (Böhringer 1994; Guzzo et al. 1995; De Grandi 1996), which started in 1992 and is still in progress. The main aim of this optical follow-up program is the spectral confirmation and measurement of the recession velocity of cluster candidates selected from RASS sources in the southern hemisphere. This will provide one of the largest samples of X-ray identified clusters, which will be an ideal tool to map the large scale structure in the Universe and investigate the evolution of clusters.

In the soft X-ray band galaxy clusters appear as single entities, as their emission originates in the thin hot plasma trapped in the deep cluster potential well. The X-ray emission of clusters, predominantly thermal bremsstrahlung, extends typically over distances on the order of a few Mpc (e.g. Sarazin 1989). A study of the properties of these objects in the X-ray band requires the existence of an algorithm that is able to characterize extended sources. By characterization we mean here the ability to determine physical quantities such as the extension and flux of a source, under conditions where the number of observed photons is low.

Previous techniques applied up to date to RASS data are the Standard Analysis Software System (SASS; Voges et al. 1992), developed at the MPE institute, and the Voronoi Tessellation and Percolation (VTP; Ebeling & Wiedenmann 1993; Ebeling 1993).

SASS uses two standard sliding window algorithms to detect the sources observed in the ROSAT survey and applies to each detection a Maximum Likelihood (ML) algorithm (Cruddace et al. 1988, Zimmermann et al. 1994) in order to derive position, source count rate, existence probability of the source, extension and probability of extension. The ML algorithm is specialized in characterizing pointlike sources as it takes into account only the point-spread function (PSF) in fitting the data. Further the PSPC point-spread function is assumed by ML, for the purpose of analytical simplicity, to be a Gaussian which depends on the energy and off-axis angle of each photon, therefore the PSF used by ML in the RASS is a sum of Gaussians (Cruddace et al. 1991). This is a raw approximation of the real survey PSF (RASS-PSF), because the sum of Gaussian PSFs does not take into account the important counts fraction contained in the wings of the real RASS-PSF (of the order of 30%). We expect that the ML algorithm, as it is applied in SASS, will lead to a systematic

underestimation of the source counts for both pointlike and extended sources and also, to an incorrect value for source extension and associated extension probability (see also Cruddace et al. 1991). In the present work we are mainly interested in the analysis of extended sources, but we believe that a discussion about the ML effects for pointlike sources is of great interest (see Appendix A).

VTP is based on concepts completely different to those of SASS. It analyses the photon distribution directly and does not assume any geometrical shape for the source emission profile in the detection process, which results in a more accurate determination of the source counts. However, this initial advantage of VTP is lost in the characterization of the detected sources, because the source emission profile is modeled using a radially symmetric profile (Ebeling et al. 1996). Moreover, no errors are associated to the VTP extensions (see Ebeling et al. 1996), this makes interpretation of the results difficult. Another limitation of VTP as applied in the RASS (i.e. Ebeling 1993; Ebeling et al. 1996) is that it has only been run in the broad band (0.1-2.4 keV). However the best ROSAT energy band for the study of clusters of galaxies is the hard band (0.5-2.0 keV), because this is the band in which the signal-to-noise ratio is maximized.

A general criticism of the ML and VTP techniques is the non optimal use of the survey PSF and the inefficiency in producing a useful extension parameter. Attempts to solve these problems have been made in the past, using observations of clusters of galaxies by earlier satellites, e.g., Lea & Henry (1988).

The ideal RASS analysis technique for extended sources should: 1) characterize in an adequate manner the source surface brightness profile, 2) use the correct survey PSF, 3) measure the clusters fluxes in the ROSAT hard band (0.5-2.0 keV), 4) discriminate between pointlike and extended sources in a sensitive manner, 5) assign a meaningful physical extension and an extension probability to each source, and, 6) use simple concepts and require little processing time for each source. The present paper is dedicated to the development of a new technique that fulfills all these requirements, the Steepness Ratio Technique (SRT).

In section 2 we will develop the theory of the SRT starting from the convolution between the real RASS-PSF and a source emission profile and we will describe how to derive extension (subsection 2.1) and flux (subsection 2.2) for RASS clusters of galaxies. In subsection 2.3 we will check the dependence of the SRT results on the parameters of the assumed source emission profile.

In order to test the reliability of the SRT we will apply, in section 3, the SRT to control samples of optically identified RASS sources and to a sample of ROSAT-PSPC pointed

observations of clusters of galaxies (subsections 3.2 and 3.3). In subsection 3.2 we develop a general criterion for discriminating between pointlike and extended RASS sources, and a way to associate an extension probability to the sources. Section 4 will summarize the principal results and conclusions.

In subsequent papers of this series (De Grandi et al. in preparation) we shall apply the new SRT to the sample of prominent southern sky galaxy clusters being studied by the ESO Key Program Redshift Survey mentioned above, in order to select an X-ray flux limited sample of bright clusters and to investigate its properties. Of prime interest is the X-ray luminosity function.

## 2. Theory of the Steepness Ratio Technique (SRT)

A proper analysis of extended sources requires that the blurring introduced by the spatial resolution of the observing instruments be taken into account correctly. This is particularly true for the RASS, where the PSF is considerably broader than the on-axis PSF for PSPC pointed observations.

During the RASS, the satellite scanned the sky along great circles perpendicular to the sun position and intersecting the ecliptic poles, with a progression rate of  $\sim 1^\circ$  per day. During each orbit, the instrument scanned a region of the sky  $\sim 2^\circ$  wide and  $360^\circ$  long at a constant ecliptic longitude. As a consequence of this observing strategy each source entered the field of view of the PSPC once per orbit, and at a slightly different position during each orbit. Therefore each source was observed at all off-axis angles in the detector. The RASS-PSF has been numerically computed at three different energies (0.3, 1.0, 2.0 keV) by averaging the PSF of the (XMA + PSPC)<sup>5</sup> PSF over all the detector, weighting the contribution from each off-axis angle with the appropriate energy-dependent vignetting factor (Hasinger, private communication). This RASS-PSF has been subsequently tested by us on a sample of bright pointlike RASS sources randomly distributed over the sky. These tests indicate that the RASS-PSF is in good agreement with the data. In Figure 1 we compare the on-axis PSF, as available in the EXSAS package (Zimmermann et al. 1994), with the RASS-PSF both computed at 1 keV. We note that the shape of the RASS-PSF cannot be described with a Gaussian function because of the pronounced wings. Inspection of Figure 1 shows that a significant fraction of the source counts for a pointlike source is found at large radii, so that one cannot neglect the effect of the RASS-PSF when studying

---

<sup>5</sup>The X-ray mirror assembly (XMA) + PSPC PSF is the point-spread function obtained by the convolution of the XMA-PSF with the PSPC-PSF.

moderately extended sources (i.e.  $r_c \lesssim 10'$ ). The ML algorithm implemented in the SASS approximates the survey PSF with a sum of Gaussian PSFs and the result is a systematic underestimation of the source fluxes both for extended and pointlike objects (see Appendix A). In the following we describe a new technique which properly takes into account the RASS-PSF.

Let us assume a reference system in polar coordinates  $(r_0, \varphi)$  with origin at the point O (see Fig. 2). Let  $I(r_0, \varphi)$  be the emission profile of a source, centered at the origin O. The flux emitted from an elementary area  $dS$  at a projected distance  $r_0$  from O and at an angle  $\varphi$  with respect to the line  $\overline{OP}$ , is given by  $I(r_0, \varphi)r_0 dr_0 d\varphi$ . Due to the PSF the flux fraction emitted from  $dS$  and observed at any point P at a distance  $r$  from the origin is <sup>6</sup>

$$I(r_0, \varphi) r_0 dr_0 d\varphi PSF(d) \quad (1)$$

where  $d$  is the distance between  $dS$  and P. Therefore, the total flux observed at P is obtained by integrating over the whole surface the contributions from the elementary areas  $dS$ :

$$\tilde{I}(r) = \int_0^\infty dr_0 \int_0^{2\pi} d\varphi I(r_0) r_0 PSF(d), \quad (2)$$

where the distance  $d$  is given by

$$d = r_0 \left[ \left( \frac{r}{r_0} - \cos \varphi \right)^2 + \sin^2 \varphi \right]^{1/2}. \quad (3)$$

We assume the surface brightness profile of clusters to be described adequately by an isothermal  $\beta$ -model (Cavaliere & Fusco-Femiano 1976; Jones & Forman 1984):

$$I(r_0) = I_0 \left[ 1 + \left( \frac{r_0}{r_c} \right)^2 \right]^{-3\beta+1/2}, \quad (4)$$

which is a function of the central surface brightness,  $I_0$ , the core radius,  $r_c$  and the  $\beta$  parameter.

As most of the RASS sources have a low photon count ( $\lesssim 100$  counts), it is not feasible to determine simultaneously all the three parameters describing the  $\beta$ -model. Previous work (e.g., Jones & Forman 1984) has shown that  $\beta$  is only moderately scattered around a mean of  $\beta = 2/3$ , and therefore we fix the  $\beta$  parameter at this value. Substituting eq. (4),

---

<sup>6</sup>We use the ROSAT All-Sky Survey PSF (RASS-PSF) computed at the energy of 1 keV. As we will show later (section 2.1), the effect of the energy dependence of the RASS-PSF on our results is negligible.

for  $\beta = 2/3$  into eq. (2) we find

$$\tilde{I}(r) = \frac{1}{2\pi r_c^2} \int_0^\infty \int_0^{2\pi} \left[ 1 + \left( \frac{r_0}{r_c} \right)^2 \right]^{-3/2} PSF(d) r_0 dr_0 d\varphi \quad (5)$$

where both the  $\beta$ -model and the PSF are normalized to unity.

A detailed study on the dependence of the technique results upon the  $\beta$  parameter is given in section 2.3.

In the following we shall illustrate, by means of two examples, why in the analysis for an extended source in the ROSAT survey 1) it is crucial not to neglect the effect of the PSF and 2) it is fundamentally important to consider the real RASS-PSF and not a Gaussian approximation.

First we solve numerically the integral in eq. (5) using a Gaussian PSF with the same FWHM used in SASS analysis of RASS data ( $96''$ , corresponding to  $\sigma = 40.85''$ ). The convolved profile,  $\tilde{I}_g(r)$ , is a function of the ratio between the core radius and the  $\sigma$  of the Gaussian PSF: when  $r_c/\sigma \ll 1$  the convolved profile tends to the PSF, while, when  $r_c/\sigma \gg 1$ , the effect of the convolution becomes negligible and  $\tilde{I}_g(r)$  tends to the  $\beta$ -model profile. In Figure 3 we show the difference between the convolved profile,  $\tilde{I}_g(r)$ , and the unconvolved  $\beta$ -model profile,  $I(r)$ , normalized to the latter (i.e.,  $(\tilde{I}_g(r) - I(r))/I(r)$ ) for three values of the  $r_c/\sigma$  ratio. In Figure 3a we illustrate the case  $r_c/\sigma = 0.01$  (i.e.,  $r_c/\sigma \ll 1$ ), here the convolved profile approximates the PSF which has a very different shape from the  $\beta$ -model profile. Consequently the quantity  $(\tilde{I}_g(r) - I(r))/I(r)$  represented in Figure 3a is very different from zero. On the contrary in Figure 3c, where  $r_c/\sigma = 100$  (i.e.,  $r_c/\sigma \gg 1$ ), the convolved profile approximates the  $\beta$ -model and the quantity  $(\tilde{I}_g(r) - I(r))/I(r)$  is always very close to zero.

In the intermediate cases, when  $r_c$  and  $\sigma$  are comparable, the convolved profile,  $\tilde{I}_g(r)$ , differs significantly from both the unconvolved and the PSF profiles. Since the effect of the convolution is to broaden the profile and both the convolved and unconvolved profiles are normalized to unity, we have that the convolved profile is weaker than the unconvolved one at small radii and vice versa is stronger for large radii (see Fig. 3b). Therefore, in studying RASS sources with core radii of the same order of magnitude of  $\sigma$  the convolution of the PSF must be taken into account.

In the second example we compare the Gaussian PSF convolved profile with the RASS-PSF convolved profile. Figure 4a shows the product of  $\tilde{I}(r) r$  as a function of the radius, for a ratio  $r_c/\sigma = 3$ . The solid line is the product computed for the RASS-PSF convolved profile, whereas the dashed line is the product computed using the Gaussian PSF. As the convolved profiles are normalized to unity, i.e.  $2\pi \int_0^\infty r \tilde{I}(r) dr \equiv 1$ , the areas

below the curves in Figure 4a are equal. The spreading effect of the convolution on the source emission profile is larger in the case of the RASS-PSF (solid line in Fig. 4a) than in the case of a Gaussian PSF (dotted line). Figure 4b shows the ratio  $(\tilde{I}(r) - \tilde{I}_g(r))/\tilde{I}_g(r)$  as a function of the radius  $r$ , where  $\tilde{I}(r)$  is the profile convolved with the RASS-PSF and  $\tilde{I}_g(r)$  the profile convolved with a Gaussian PSF. The profiles differ significantly and the ratio is larger than 10% for radii larger than  $4'$ , indicating that it is not possible to approximate the real PSF with a simple Gaussian function.

## 2.1. Extension

Once the RASS-PSF convolved  $\beta$ -model profile has been derived it can be used to extract information on the extension of RASS sources. Since the objects observed during the survey are characterized by low statistics, we choose to compare the convolved profile (5) with the data using integrals of  $\tilde{I}(r)$ . In particular, we integrate eq. (5) in a circle with a radius of  $3'$  and in an annulus bounded by the two radii  $3'$  and  $5'$ , obtaining the counts fractions

$$\begin{aligned} C(3') &= 2\pi \int_0^{3'} r \tilde{I}(r) dr; \\ C(5' - 3') &= 2\pi \int_{3'}^{5'} r \tilde{I}(r) dr. \end{aligned} \quad (6)$$

Now we consider the ratio between the two above integrals:

$$SR \equiv \frac{C(5' - 3')}{C(3')}. \quad (7)$$

We name this quantity the steepness ratio ( $SR$ ), as it is a measure of the slope of the convolved profile  $\tilde{I}(r)$ . There is a strong analogy between the steepness ratio, which we will use in deriving the extension of the sources, and the hardness ratio used as a measure of the spectral slope. In both cases photon counts are accumulated into two bins, as a result of the limited statistics of the sources.

As  $SR$  is a monotonic function of the core radius  $r_c$ , (Fig. 5) it may be used to obtain the core radius from the observed steepness ratio,  $SR_{\text{obs}}$ . The  $SR_{\text{obs}}$  is measured from the survey data as the ratio between the source counts falling into a  $3'$  radius circle and the source counts falling into an annulus bounded by the two radii of  $3'$  and  $5'$ :

$$SR_{\text{obs}} = \frac{cts(5' - 3')}{cts(3')}. \quad (8)$$

The uncertainty in measuring  $SR_{\text{obs}}$  is computed applying the usual formulae for error propagation, using the errors in the two independent quantities  $cts(3')$  and  $cts(5' - 3')$ . The

$SR - r_c$  curve is applied to compute the errors in the derived core radius, using the known errors in  $SR_{\text{obs}}$ .

In Figure 5 we also illustrate the case of the  $SR - r_c$  curve computed from an unconvolved  $\beta$ -model profile (dotted curve). The ratio  $(SR_{\bar{I}} - SR_I)/SR_I$  between the RASS-PSF convolved and unconvolved  $SR - r_c$  curves is shown in Figure 6. As can be clearly seen in Figure 6 the two curves, drawn in Figure 5, are quite different and only for core radii larger than  $11'$  do they differ by less than 1%, while at  $2'$  the difference is  $\sim 50\%$ .

To examine the energy dependence of the  $SR - r_c$  curve, we have computed different  $SR - r_c$  curves using the RASS-PSF at 0.3 keV and 2.0 keV. The ratios between the curves, computed at different energy, is never greater than 2% for  $r_c \lesssim 10''$  and it is always less than a few 0.1 percent at larger core radii. We conclude that the energy dependence of the curve  $SR - r_c$  is negligible.

At core radii  $r_c \lesssim 10''$  the convolved profile (eq. 5) approaches the RASS-PSF. Consequently, as shown in Figure 5, the  $SR$  becomes insensitive to the core radius and approaches the value 0.15, which is characteristic of pointlike sources (see eq. 7). For very large  $r_c$ , the dominant profile is that of the  $\beta$ -model and the photons distribution between  $0'$  and  $5'$  is practically flat so that the  $SR - r_c$  curve tends to the constant value 1.78 (i.e., the ratio of the areas of the annulus ( $5' - 3'$ ) and the circle of radius  $3'$ ). As a corollary at large ( $r_c > 1000''$ ) and small ( $r_c < 40''$ ) radii, small variations of  $SR$  lead to large variations in the core radius, thus in these regions the  $SR - r_c$  curve is not suitable to measure the core radius. On the other hand when the derivative of  $SR$  with respect to  $r_c$  is large (i.e. in the range  $60'' \lesssim r_c \lesssim 900''$ ), the curve provides a good estimation of the core radius. For a typical cluster, with physical core radius of 250 kpc (e.g., Bahcall 1975), this corresponds to a redshift range of  $0.009 < z < 0.2$  ( $H_0 = 50$  km/s/Mpc).

A different choice for the radii of the circle and the annulus, results in a new  $SR - r_c$  curve, and changes the range in which  $r_c$  can be derived adequately. Inspection of Figure 5 shows that  $SR = 1$  for  $r_c \sim 200''$ . Had we chosen a significantly larger circle and annulus,  $SR$  would have been equal to 1 for a larger core radius and therefore would be inadequate to characterize barely extended sources. A significantly smaller circle and annulus would allow us to characterize such sources, but would provide poor information for more extended objects.



## 2.2. Total Source Counts

In the case of a pointlike source it is possible to compute the source counts by counting the events within a circle of a fixed extraction radius and then correcting for the counts falling outside that radius using the PSF. In the case of an extended sources this correction must take into account the source extension, using the following procedure.

Consider a source for which we have obtained the core radius using the SRT. As the RASS-PSF convolved emission profile in eq. (5) is normalized so that  $2\pi \int_0^\infty r \tilde{I}(r) dr \equiv 1$ , the total source counts are given by

$$cts_{tot} = cts(5') F, \quad (9)$$

where  $cts(5')$  are the observed source counts in  $5'$ , and

$$F = \frac{1}{2\pi \int_0^{5'} r \tilde{I}(r) dr}. \quad (10)$$

The correction factor  $F$  is a function dependent only on  $r_c$ ,  $\beta(=2/3)$  and the PSF. As the steepness ratio (eq. 7) is likewise a function of these three quantities, it follows that  $F$  is a function of  $SR$ , as shown in Figure 7.

The  $SR - F$  curve can be used to compute the errors in the derived correction factor  $F$ , from the errors on  $SR_{obs}$ . The uncertainties ascribed to the total source counts,  $cts_{tot}$ , are computed applying the usual formulae for error propagation, using the errors in the two independent quantities  $cts(5')$  and  $F$ . In Figure 7 we also show the  $SR - F$  curve computed using an unconvolved  $\beta$ -model profile (dotted curve). The ratio  $(F_1 - F_1)/F_1$  between the RASS-PSF convolved and unconvolved curves, drawn in Figure 8, shows significant differences in the derived total flux. Only for core radii larger than about  $14'$  do they differ by less than 5%, while at  $3'$  the difference is  $\sim 12\%$ .

To study how the energy dependence of the RASS-PSF impacts the  $SR - F$  curve we have recomputed the  $SR - F$  curve using the 0.3 and 2.0 keV RASS-PSF. We find that the ratio between the nominal curve, computed at 1 keV, and either of the other two curves is never greater than 3% and therefore conclude that the energy dependence of the RASS-PSF has a negligible effect upon the computation of the total source counts.

At small core radii,  $r_c < 10''$ , the correction factor  $F$  tends to 1.049 (Fig. 7), i.e. the inverse of the RASS-PSF integral between 0 and  $5'$ . This limit is the correction that has to be applied for pointlike sources, this implies that SRT can also be used to compute total source counts for pointlike sources. On the other hand at very large core radii,  $r_c > 1000''$ , the correction factor  $F$  increases indefinitely, so that, as in the case of the core radius, the SRT is not applicable to objects with very large core radii ( $r_c \gtrsim 1000''$ ).

### 2.3. Dependence of the SRT Results upon the $\beta$ Parameter

One of the fundamental hypotheses which the SRT is based on is the assumption of a fixed value for the  $\beta$  parameter,  $\beta = 2/3$ . We investigate now how this hypothesis could affect the measure of the core radius and of the total counts of a RASS source. In previous work (e.g., Jones & Forman 1984) it has been found that the value of the  $\beta$  parameter for galaxy clusters ranges between  $\sim 3/5 - 4/5$ . Therefore, we recompute the  $SR - r_c$  and  $SR - F$  curves for the two limiting values  $3/5$  and  $4/5$  for  $\beta$ , and compare them with the curves computed for  $\beta = 2/3$ .

#### 2.3.1. Core Radii

The  $SR - r_c$  curves computed for a RASS-PSF convolved  $\beta$ -model for  $\beta$  equal to  $3/5$ ,  $2/3$  and  $4/5$  are plotted in Figure 9. The  $SR$  of the three curves tend to the same limits for small and large  $r_c$ , and the core radius derived for  $\beta = 2/3$  always lies between the values of  $r_c$  obtained for  $\beta = 3/5$  and  $4/5$ . Using the curves in Figure 9 we compute the following ratios:

$$\begin{aligned} \Delta r_c(\beta = 3/5, \beta = 2/3) &\equiv \frac{r_c(SR, \beta = 3/5) - r_c(SR, \beta = 2/3)}{r_c(SR, \beta = 2/3)}, \\ \Delta r_c(\beta = 4/5, \beta = 2/3) &\equiv \frac{r_c(SR, \beta = 4/5) - r_c(SR, \beta = 2/3)}{r_c(SR, \beta = 2/3)}. \end{aligned} \quad (11)$$

In Figure 10 these ratios are plotted as a function of the core radius obtained for  $\beta = 2/3$ . As we will show in the next section (3.), values of  $r_c(SR, \beta = 2/3)$  below  $50''$  are not interesting, because for these values is not possible to distinguish between pointlike and extended RASS sources. Figure 10 shows that the largest difference in the core radius ( $\sim 50\%$ ) is found for  $r_c = 50''$ , and the differences decrease as the core radius increases, falling to  $\sim 7\%$  at  $r_c \sim 1000''$ . The difference in the core radii found at small values, near  $50''$ , depends upon the radii chosen for the circle and the annulus used in eq. 7.

#### 2.3.2. Total Source Counts

We consider now how different  $\beta$  parameter values could affect the total source counts. Analogous to the procedure shown in the previous section we compute the  $SR - F$  curves for  $\beta = 3/5$ ,  $2/3$  and  $4/5$ , yielding the results shown in Figure 11. We define the ratios:

$$\Delta F(\beta = 3/5, \beta = 2/3) \equiv \frac{F(SR, \beta = 3/5) - F(SR, \beta = 2/3)}{F(SR, \beta = 2/3)},$$

$$\Delta F(\beta = 4/5, \beta = 2/3) \equiv \frac{F(SR, \beta = 4/5) - F(SR, \beta = 2/3)}{F(SR, \beta = 2/3)}. \quad (12)$$

These ratios are plotted in Figure 12 as a function of the core radius  $r_c(SR, \beta = 2/3)$ . At small core radii these ratios tend to zero, as the correction factor  $F$  approaches that found for pointlike sources. The ratios increase with increasing core radius, reaching a maximum value of  $\sim 30\%$  when the core radius is about  $1000''$ .

We conclude that the assumption  $\beta = 2/3$  could lead to an error in the derived total source counts ranging from 0 to 30%.

### 3. Applying the SRT to Control Samples

The reliability of the SRT has been tested using different control samples of optically identified sources observed in the RASS. These samples represent an alternative to the use of simulated RASS fields. Indeed a ROSAT observation, carried out during the survey, is the result of complex scan operations and often is influenced by random events, for example the PSPC switching off during the passage through intense charge particles zones (i.e. the South Atlantic Anomaly), attitude problems occurring during some scans, and scan reversals every 30 days, which were made to avoid earth occultations. For these reasons realistic simulations of RASS observations are hard to plan. Therefore we preferred to use control samples of real RASS sources, which take into account directly all the observational difficulties present in the survey.

Our control samples are: 1) the EMSS sample (Gioia et al. 1990, Maccacaro et al. 1994) reobserved in the RASS, 2) an all-sky sample of 262 bright RASS stars selected by correlating the SASS source list (Voges 1992) with the SIMBAD database at the Centre de Donnes Astronomiques de Strasbourg, and yielding more than 100 SASS counts in the hard band (0.5-2.0 keV), and 3) a sample of 26 Abell clusters (Abell et al. 1989) extracted from the public archive of deep ROSAT-PSPC pointed observations.

#### 3.1. Data Analysis

We analyze RASS fields of  $2^\circ \times 2^\circ$ , centered on the SASS sources positions. The data are produced by merging all the RASS scans at a position in the sky. An automatic analysis procedure has been developed that uses the spatial analysis techniques available within the EXSAS (Zimmermann et al. 1994) package. The algorithm: 1) applies a local source

detection (LD) algorithm to the binned data,<sup>7</sup> 2) produces a “swiss-cheesed” image which is obtained by removing the events from  $5'$  circles centered on the detected source positions,<sup>8</sup> 3) computes a background map of the field by performing a 2-dimensional cubic spline fit of the “swiss-cheesed” image, 4) applies the Maximum Likelihood algorithm (ML) to the unbinned data, deriving a position, an existence likelihood, a count rate, an extension and an extension likelihood for the source at the center of the field, 5) extracts the source counts in a  $3'$  circle and in an  $(5' - 3')$  annulus centered on the position found by the ML algorithm and 6) applies the SRT deriving an extension ( $r_c$ ), an extension probability (see section 3.2) and the total source counts ( $cts_{tot}$ ). This procedure is applied independently using each of the three ROSAT energy bands, i.e. the broad (0.1-2.4 keV), soft (0.1-0.4 keV) and hard (0.5-2.0 keV) bands.

### 3.2. Separating Extended from Pointlike Sources

We consider the EMSS subsample of 30 RASS bright sources, obtained by selecting objects with more than 100 counts in the ROSAT hard band (0.5 - 2.0 keV) within a  $5'$  radius circle around the ML position. In Figure 13 we show the distribution of core radius for this subsample. The pointlike sources (dashed histogram) have core radii smaller than  $\sim 50''$ , with the only exception indicated by the black bar. This object is the BL-Lac MS1207.9+3945 which is located  $\sim 5'$  from one of the brightest AGN in the sky NGC4151. The spatial resolution of the RASS does not allow to separate MS1207.9+3945 from NGC4151. The extended sources, clusters of galaxies and galaxies (white histogram), clearly show a distribution that is different from that of pointlike sources. The SRT core radii distribution for the control sample of 262 bright stars identified using SIMBAD is shown in Figure 14. The distribution decreases rapidly at radii smaller than  $20''$  and goes to zero at about  $60''$ .

In the following we develop a general criterion for discriminating between pointlike and extended RASS sources. Such a criterion is extremely useful in the preidentification phase of RASS sources, i.e. once a RASS source is recognized as being extended, it can belong only to a few astrophysical classes of objects. Moreover, in the case of sources localized beyond the galactic plane, the most probable classes of extended objects are galaxies and

---

<sup>7</sup>If the detection algorithm finds a secondary emission peak within a  $10'$  radius from the primary peak, then the source is flagged.

<sup>8</sup>in the case of the central source, which may be extended, we cut out a circle with a radius of  $24'$ , to avoid contamination of the background from the halo of a possibly extended source.

clusters of galaxies.

We consider the control sample of bright stars and the EMSS pointlike objects identified as stars or AGN. In order to have a fair sample of very bright pointlike sources, we selected in both samples only those sources with more than 100 hard band (0.5-2.0 keV) counts within a  $5'$  radius circle. In total we obtain 286 bright pointlike sources.

For these sources we define the observed distribution of  $SR$  as  $dn_{occ}(SR)/dSR$ , where  $dn_{occ}$  is the occurrence number for  $SR$  in the interval  $dSR$ . Normalizing to the total number of objects,  $n_{occ}$ , we obtain the observed probability density:

$$\frac{dP_{obs}}{dSR} = \frac{1}{n_{occ}} \frac{dn_{occ}(SR)}{dSR}. \quad (13)$$

A cubic spline-fit algorithm applied to the distribution (13) leads to a continuous representation of the probability density function,  $dP/dSR$ , and the distributions  $dP_{obs}/dSR$  and  $dP/dSR$  are shown in Figure 15. The two distributions peak at a low value of  $SR$  around 0.17, and then fall rapidly to zero for values of  $SR$  greater than 0.3.

We use now the  $dP/dSR$  curve to associate an extension probability for each RASS source. The case of sources with negligible errors is considered first, after which errors are included. Consider a source with an observed steepness ratio,  $SR_{obs}$ . The probability for a pointlike source to have a steepness ratio greater or equal to  $SR_{obs}$ , is given by:

$$P(\geq SR_{obs}) = \int_{SR_{obs}}^{\infty} \frac{dP}{dSR} dSR. \quad (14)$$

As shown in Figure 15, the greater the value of  $SR_{obs}$  the smaller is the probability  $P(\geq SR_{obs})$  for a source with  $SR \geq SR_{obs}$  to be pointlike. Equation (14) is valid if the error,  $\sigma_{SR_{obs}}$ , is small with respect to  $SR_{obs}$ . However if  $\sigma_{SR_{obs}}$  is not negligible, we must take into account the probability distribution,  $dG/dSR$ , associated with the measured  $SR_{obs}$ . A Gaussian distribution of errors is assumed:

$$\frac{dG}{dSR} = \frac{1}{\sigma_{SR_{obs}} \sqrt{2\pi}} \exp \left[ -\frac{1}{2} \left( \frac{SR - SR_{obs}}{\sigma_{SR_{obs}}} \right)^2 \right] \quad (15)$$

The analog of eq. (14) is obtained weighting the probability  $P(\geq SR_{obs})$  over the probability distribution  $dG/dSR$  of the source, giving

$$P(\geq SR_{obs}) = \int_0^{\infty} dSR' \frac{dG}{dSR'} \int_{SR'}^{\infty} dSR \frac{dP}{dSR}. \quad (16)$$

When  $\sigma_{SR_{obs}}/SR_{obs} \rightarrow 0$  the Gaussian given in eq. (15) tends to a Dirac function, and eq. (16) turns into eq. (14).

We can now use the probability defined in eq. (16) to test our null order hypothesis (i.e. that an X-ray source belongs to a population of pointlike objects). Therefore, we call “extended” those sources having an associated probability,  $P(\geq SR_{\text{obs}})$ , as defined in eq. (16), smaller than 0.01. In the case of a source with an error  $\sigma_{SR_{\text{obs}}}$  negligible with respect to  $SR$ , a probability of 0.01 corresponds to  $SR = 0.334$ .

### 3.3. Checking the SRT Source Count Rates

#### 3.3.1. Checking Count Rates for Pointlike Sources

To check the accuracy of the SRT in determining the source count rates, we consider all the 131 EMSS pointlike objects identified as stars or AGN detected in the RASS (i.e., we do not apply any cut in source counts). Moreover, we use the source counts instead of the count rates, because counts show more clearly statistical effects.

By integrating the RASS-PSF at 1 keV between  $0'$  and  $5'$  we find that the expected counts fraction falling in a circle of  $5'$  radius from the RASS-PSF peak is 95.3%. Therefore the ratio  $(cts_{\text{tot}} - cts(5'))/cts(5')$ , where  $cts_{\text{tot}}$  and  $cts(5')$  are respectively the total source counts (eq. 9) and the counts in  $5'$ , expected for a pointlike source is 0.05. Averaging the above ratio over the whole distribution of pointlike EMSS sources, we find that it is consistent with the expected value ( $0.06 \pm 0.015$ ).

As we pointed out previously SRT is a technique specifically developed to characterize RASS sources when the photon statistics is low. In the following we investigate how SRT performs as a function of the signal-to-noise ratio of detection.

In the analysis of the EMSS pointlike sources we find that for a fraction of them (23/131) SRT is not able to compute core radius nor total source counts. This occurs when the statistical fluctuations of the counts in circles of  $3'$  and  $5'$  radii give unphysical  $SR$  (eq. 7), e.g., when the counts within  $3'$  are larger than those within  $5'$ . To quantify this effect we define the signal-to-noise ratio as the ratio between the source counts measured within a circle of  $5'$  radius and the square root of the total counts (i.e., source + background) measured in the same circle, and we study the capability of SRT to characterize RASS sources as a function of the signal-to-noise. We find that SRT does not miss any EMSS pointlike sources, due to an unphysical  $SR$  value, when the signal-to-noise ratio is larger than 4. This corresponds to  $\sim 20$  source counts within  $5'$ . For signal-to-noise ratios equal to 3, 2 and 1 the technique fails respectively in the  $8\% \pm 6\%$ ,  $45\% \pm 14\%$  and  $33 \pm 19\%$  of cases. The source photon counts into  $5'$  associated with signal-to-noise of 3, 2 and 1 are small, i.e.  $\sim 15$ , 10 and 5 respectively.

Finally we investigate how well SRT estimates the flux of pointlike sources as a function of the signal-to-noise ratio. We consider again the ratios  $(cts_{\text{tot}} - cts(5'))/cts(5')$  defined above, and we compute the weighted means of these ratios averaged on bins of signal-to-noise. We find that the means are always consistent with the expected value, within less than a few 0.1%. Therefore the count rates estimated by SRT are not affected by systematical errors at any signal-to-noise ratio.

### 3.3.2. Checking Count Rates for Extended Sources

In this section the SRT count rates obtained from RASS data are compared with count rates measured from ROSAT-PSPC pointed observations of a sample of 26 Abell clusters of galaxies, which we have analyzed using the EXSAS package. We sum the counts in a circle of appropriate radius centered on the cluster emission peak and subtract the background estimated in a region void of sources. As the majority of the clusters are significantly extended, we consider vignetting by weighting each photon with the PSPC response function at the appropriate off-axis angle and energy. We obtain the count rates by dividing the source counts by the exposure time of the observation.

In Figure 16 we show the relation between the RASS-SRT and the pointed observations count rates. The uncertainties in the count rates are 1-sigma errors, and both count rates are computed in the hard band (0.5-2.0 keV). The correlation between the two independent quantities is good and is valid for a large dynamic range, i.e. count rates range from  $\sim 0.3$  to 4 cts/s. The SRT leads to significantly different count rates in the case of three clusters only (A2877, A3376 and A3266). A detailed analysis of the pointed data showed that, in all three cases, the real emission profile of the source differed significantly from a  $\beta$ -model profile with  $\beta = 2/3$ , because of the very peculiar morphology or asymmetry of the cluster.

Note that, the hypothesis of radial symmetry of the sources, implemented in the SRT, does not introduce any systematic bias in the measured count rates. Very extended RASS clusters which are not fitted well using the  $\beta$ -model with  $\beta = 2/3$ , can exhibit widely differing steepness ratios values (see eq. 8), because the photons in  $3'$  and  $5'$  can be distributed in many ways, depending on the cluster morphology. Under these circumstances the SRT may lead to either an under- or overestimation of the count rate. In the case of clusters with extension comparable with the FWHM of the RASS-PSF, the inhomogeneities are blurred significantly by the RASS-PSF, so that deviations of the intrinsic source profiles from the radial symmetry are less important. As pointed out in De Grandi (1996) and we will show in the next paper of this series (De Grandi et al. in preparation) the majority of clusters observed in the ROSAT survey have extensions comparable with the size of the

RASS-PSF. Therefore SRT will derive an incorrect count rate for a minority of significantly extended clusters only.

Figure 16 shows that no correction to the SRT count rate is necessary, unlike the techniques used to date. For example the VTP technique (Ebeling & Wiedenmann 1993), which computed the RASS count rates in the ROSAT broad band only, is affected significantly by the presence of X-ray pointlike sources within clusters and therefore requires correction for contamination of the RASS count rates on a statistical basis (Ebeling et al. 1996).

Finally we quantify how the SRT count rate measure holds for RASS extended sources as a function of the signal-to-noise ratio of detection. We use the signal-to-noise ratio as defined in section 3.3.1 and the EMSS sources identified with galaxies and galaxy clusters detected in the hard band RASS data (21 objects). We find that in no case SRT fails to characterize the sources, due to an unphysical value of  $SR$ , for signal-to-noise  $\gtrsim 3$  (corresponding to about 10 – 20 source counts within 5'). Moreover, we have checked the validity of the SRT count rates as a function of the signal-to-noise for the extended sources using the independent data set of the ROSAT-PSPC pointed observations for the 26 Abell clusters mentioned above. For each Abell cluster we compute the ratio  $(cts_{\text{tot}} - cts_{\text{point}})/cts_{\text{point}}$ , where  $cts_{\text{tot}}$  and  $cts_{\text{point}}$  are respectively the RASS total source counts (eq. 9) and the counts measured from the pointed observations, and then we compute the averaged mean of these ratios in signal-to-noise bins. We verify that for signal-to-noise  $\gtrsim 5$  (corresponding to about 25 – 35 source counts within 5') the mean value of the ratio is always within  $\sim 1\%$  of the expected value.

#### 4. Conclusions

The new steepness ratio technique developed in this paper is particularly suitable to characterize the extended RASS sources in conditions of low signal-to-noise ratio. For the first time in the RASS clusters of galaxies analysis, this technique convolves the source surface brightness profile and the real point-spread function of the ROSAT survey. We have verified that a Gaussian approximation of the PSF, as implemented in the standard RASS analysis software (SASS) leads to an underestimation of the source counts (i.e. fluxes) both for pointlike and extended sources. In the SRT we assume a model describing the surface brightness profile of clusters of galaxies, namely the  $\beta$ -model with the  $\beta$  parameter fixed to the value of 2/3. In previous work (e.g., Jones & Forman 1984) it has been found that the  $\beta$  parameter for galaxy clusters is moderately scattered around a mean of 2/3. Therefore we have performed a detailed study of the dependence of the SRT results upon



the  $\beta$  parameter, which shows that a fixed  $\beta = 2/3$  could in extreme cases lead to errors on the total source counts of no more than 30%.

We tested the reliability of the SRT applying the new technique on control samples of optically identified X-ray sources. The most important test has been the comparison of the SRT count rates computed from RASS data with the count rates computed from deep ROSAT-PSPC pointed observations, both measured in the hard band (0.5-2.0 keV), for a sample of Abell clusters of galaxies. We found good agreement, implying that no corrections to the SRT count rates are necessary.

All the tests we have performed lead to the conclusion that the steepness ratio technique is a robust estimator of the flux for the RASS clusters of galaxies and pointlike sources. Using the steepness ratio (SR) and a control sample of RASS pointlike sources we were able to assign to each RASS source a model-independent probability of extension.

In the following papers of this series we will apply the SRT to a defined sample of galaxy clusters candidates, obtained from the ESO Key Program Redshift Survey of southern sky clusters, in order to select an X-ray flux-limited sample of bright clusters and to investigate in detail the X-ray properties of this sample.

SD would like to thank R. Cruddace for a critical reading of the manuscript. SD acknowledges also useful discussions with G. Zamorani, C. Izzo and A. Edge. The authors would like to thank G. Hasinger for having provided the numerical RASS-PSF. This work has been performed within the framework of the ESO Key Program Redshift Survey of southern ROSAT clusters, and the contribution from the project team is gratefully acknowledged.

## A. Appendix

In this section we discuss the results of the Maximum Likelihood (ML) method (Cruddace et al. 1988) applied to the survey data through the Standard Analysis Software System (Voges et al. 1992) at the MPE.

We select from the EMSS sample (Gioia et al. 1990, Maccacaro et al. 1994) a subsample of 131 pointlike sources (i.e. optically identified AGN, BL-Lac and stars) which were reobserved in the RASS and derive for them the ML source counts from the merged data as described in section 3. As the counts fraction falling into a circle of  $5'$  radius from the the RASS-PSF peak is 95.3%, we choose to compare the ML source counts of pointlike objects,  $cts_{ML}$ , to the source counts inside  $5'$ ,  $cts(5')$  (see Fig. 17). For both methods the

source counts are measured in the broad band (0.1-2.4 keV). From Figure 17 we note two important effects: 1) the ML method systematically underestimates the source counts, and 2) the source counts underestimation is a function of the counts number and it is larger for the weaker sources. The ratio,  $(cts_{\text{ML}} - cts(5'))/cts(5')$ , averaged over the whole distribution is  $0.22 \pm 0.01$ .

The ML algorithm leads to an underestimation of the source counts of the pointlike objects because it uses a sum of Gaussian PSFs as the RASS-PSF. It is possible to explain the effect observed in Figure 17 by means of simple considerations. The surface brightness profile of a pointlike RASS source is described by the RASS-PSF, that has pronounced wings (see Fig. 1). If the source is weak, only the central part of the RASS-PSF is emerging from the local background level. Therefore, the ML method, that uses a sum of Gaussian PSFs to describe the source, is forced to fit with greater precision the part of the RASS-PSF with the better statistics, namely the core. Hence, the PSF used by the ML is not able to fit the wings of the real RASS-PSF and consequently underestimates the counts of a weak source.

On the other hand the surface brightness profile of a bright pointlike source emerges more distinctly from the local background, and the statistics in the wings is much better than in the case of a weak source. The ML algorithm includes an attempt to analyze extended sources, by which a test is made to see whether a Gaussian surface brightness profile improves the fit. This has the unfortunate result that the algorithm, working with a sum of Gaussian PSFs, interprets the wings of the real PSF as an extension of the source. Consequently, while this procedure makes a more accurate estimate of the flux from a strong pointlike source, at the same time it assigns a false extension. This is confirmed in Figure 18, which for the sample of bright stars described in section 3 shows a correlation between the total counts and the extension likelihood derived by ML.

## REFERENCES

- Abell, G. O., Corwin, H. G., Olowin, R. P. 1989, *ApJS*, 70, 1
- Bahcall, N. A. 1975, *ApJ*, 198, 249
- Böhringer, H. 1994, in *Studying the Universe with Clusters of Galaxies*, Böhringer H. & Schindler S. (eds), MPE report 256, 93
- Briel, U. G. & Pfeffermann, E. 1986, *Nucl. Instr. and Methods*, A242, 376.
- Cavaliere, A. & Fusco-Femiano R. 1976, *A&A*, 49, 137
- Cruddace, R. G., Hasinger, G. R., Schmitt, J. H. 1988, in *Astronomy from Large Database*, F. Murtagh & A. Heck (eds), 177
- Cruddace, R. G., Hasinger, G., Trümper, J., Schmidt, J. H. M. M., Hartner, G. D. 1991, *Experimental Astronomy*, 1, 365
- De Grandi, S. 1996, PhD-Thesis, University of Milan
- De Grandi, S. et al., in preparation
- Ebeling, H. 1993, PhD-Thesis, University of Munich
- Ebeling, H., & Wiedenmann, G. 1993, *Phys. Rev. E*, 47, 704
- Ebeling, H., Voges, W., Böhringer, H., Edge, A. C., Huchra, J. P., Briel, U. G. 1996, *MNRAS*, 281, 799
- Gioia, I. M., Henry, J. P., Maccacaro, T., Morris, S. L., Stocke, J. T., and Wolter, A. 1990, *ApJ*, 356, 35L
- Guzzo, L. et al. 1995, in *Wide Field Spectroscopy and Distant Universe*, Maddox S. J. & Aragon-Salamanca A. (eds), World Scientific, 205
- Hasinger, G. 1995, private communication
- Jones, C. & Forman, W. 1984, *ApJ*, 276, 38
- Lea, S. M. & Henry, J. P. 1988, *ApJ*, 332, 81
- Maccacaro, T., Wolter, A., McLean, B., Gioia, I. M., Stocke, J. T., Della Ceca, R., Burg, R., and Faccini, R. 1994, *Astro Lett. and Communications*, 29, 267

- Sarazin, C. L. 1988, X-ray Emission from Clusters of Galaxies (Cambridge Univ. Press: Cambridge)
- Stocke, J. T. et al. 1991, ApJS, 76, 813
- Trümper, J. 1993, Science, 260, 1769
- Voges, W. 1992, in Proceedings of Satellite Symposium 3, ed. T. D. Guyenne & J. J. Hunt, ESA-ISY-3 (Noordwijk:ESA), 9
- Voges, W. et al. 1992, in Proceedings of Satellite Symposium 3, ed. T. D. Guyenne & J. J. Hunt, ESA-ISY-3 (Noordwijk:ESA), 223
- Zimmermann, H. U., Becker, W., Belloni, T., Döbereiner, S., Izzo, C., Kahabka, P. & Schwentker, O. 1994, EXSAS User's Guide, MPE-Report 257

Fig. 1.— The ROSAT All-Sky Survey PSPC point-spread function (solid line) is compared with the on-axis PSPC point-spread function (dotted line). Both PSFs are computed at the energy of 1.0 keV, and normalized to unity.

Fig. 2.— Sketch of the geometry involved in computing the convolution between a source emission profile  $I$  centered in the origin O, and the point-spread function.

Fig. 3.— Ratios  $(\tilde{I}_g(r) - I(r))/I(r)$  as a function of the radius  $r$ . The quantities  $\tilde{I}_g(r)$  and  $I(r)$  are respectively, the PSF convolved and unconvolved  $\beta$ -model emission profiles. The PSF used in the convolution is a Gaussian function with  $\sigma = 40.85''$ . In (a) the convolved and unconvolved profiles are computed for a ratio  $r_c/\sigma \ll 1$ , in (b) for  $r_c/\sigma \approx 1$  and in (c) for  $r_c/\sigma \gg 1$ .

Fig. 4.— (a) Product  $\tilde{I}(r) r$  as a function of the radius  $r$ . The quantity  $\tilde{I}(r)$  is the PSF convolved  $\beta$ -model profile computed for a ratio  $r_c/\sigma = 3$ . The solid line is the profile convolved with the RASS-PSF, whereas the dashed line is the profile convolved with a Gaussian PSF with  $\sigma = 40.85''$ . The two profiles are normalized to unity, i.e. the areas below the solid and dotted lines are equal. (b) Ratio  $(\tilde{I}(r) - \tilde{I}_g(r))/\tilde{I}_g(r)$  as a function of the radius  $r$ .  $\tilde{I}(r)$  and  $\tilde{I}_g(r)$  are obtained from convolutions with the real RASS-PSF and a Gaussian PSF respectively.

Fig. 5.— The steepness ratio,  $SR$  as a function of the core radius,  $r_c$ . The solid line is the curve computed using the  $\beta$ -model convolved with the RASS-PSF, and the dotted line is computed using a simple  $\beta$ -model profile. Vertical and horizontal lines show how to derive the core radius (solid lines) from the steepness ratio and its errors (dashed lines).

Fig. 6.— The difference between the  $SR$  value computed by the RASS-PSF convolved  $\beta$ -model,  $SR_{\tilde{I}}$ , and that obtained from the unconvolved  $\beta$ -model,  $SR_I$  (cfr. Fig. 5), plotted as a function of the core radius  $r_c$ .

Fig. 7.— The dependence of the correction factor  $F$  upon the steepness ratio  $SR$ . The solid line is the curve computed using the RASS-PSF convolved  $\beta$ -model profile, and the dotted line that obtained using a simple  $\beta$ -model profile. Vertical and horizontal lines show how to derive the correction factor (solid lines) and its errors (dashed line) from steepness ratio.

Fig. 8.— The differences between the correction factor  $F$ , computed by the RASS-PSF convolved  $\beta$ -model  $F_{\tilde{I}}$ , and that obtained from the unconvolved  $\beta$ -model,  $F_I$  (cfr. Fig. 7), plotted as a function of the core radius  $r_c$ .

Fig. 9.— The  $SR - r_c$  curve computed for a RASS-PSF convolved  $\beta$ -model emission profile for different values of  $\beta$ . The solid line is for  $\beta = 2/3$ , the dotted one for  $\beta = 3/5$  and the

dashed one for  $\beta = 4/5$ .

Fig. 10.— The ratios  $\Delta r_c$ , defined in eq. (11), as a function of the core radius  $r_c$ . The solid line shows  $\Delta r_c(2/3, 2/3)$ , the dotted line  $\Delta r_c(3/5, 2/3)$  and the dashed line  $\Delta r_c(4/5, 2/3)$ .

Fig. 11.— The dependence of the correction factor  $F$  upon the steepness ratio  $SR$ . over a range of parameter  $\beta$ :  $\beta = 3/5$  (dotted line),  $2/3$  (solid line) and  $4/5$  (dashed line).

Fig. 12.— The ratio  $\Delta F$ , defined in eq. (12), as a function of the core radius  $r_c$ . The solid line shows  $\Delta F(2/3, 2/3)$ , the dotted line  $\Delta F(3/5, 2/3)$  and the dashed line  $\Delta F(4/5, 2/3)$ .

Fig. 13.— SRT core radii distribution for the 30 brightest EMSS sources. The dashed histogram shows the core radii distribution of pointlike sources, whereas the unshaded histogram shows the distribution of clusters of galaxies and galaxies. The source colored in black is the BL-Lac MS1207.9+3945 which is located  $\sim 5'$  from the very bright AGN NGC4151.

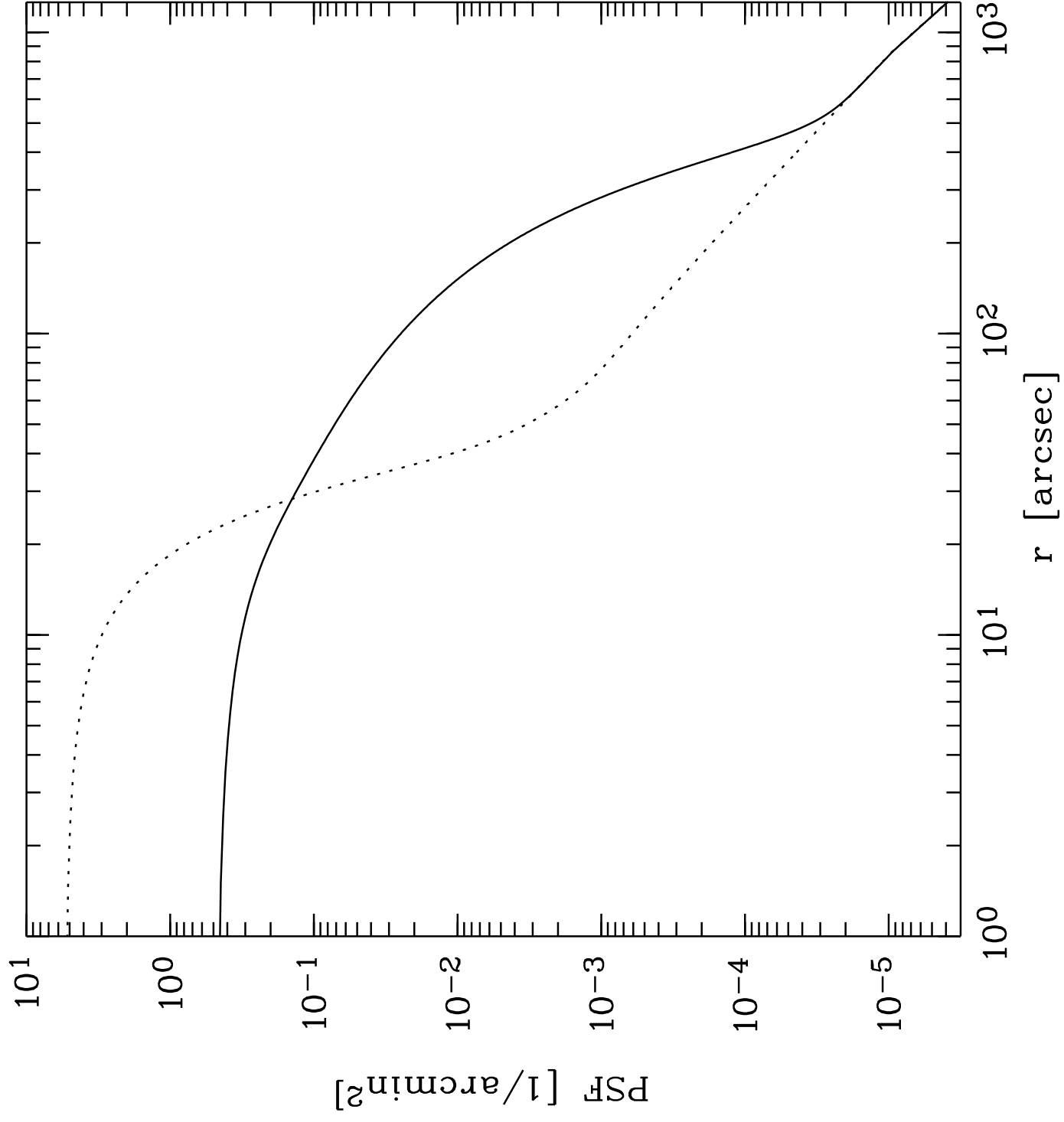
Fig. 14.— The distribution of core radii measured with the SRT for the RASS sample of bright stars.

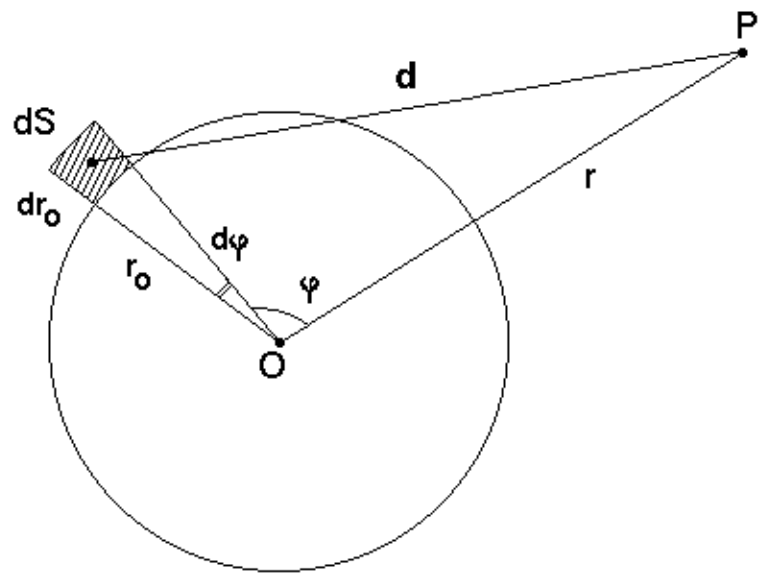
Fig. 15.— The distribution of the observed probability density,  $dP_{\text{obs}}/dSR$ , for the pointlike sources with the steepness ratio,  $SR$ . The solid line shows the  $dP/dSR$  curve obtained applying a cubic spline-fit to the observed distribution  $dP_{\text{obs}}/dSR$ .

Fig. 16.— A comparison between the count rates of 26 bright Abell clusters measured from ROSAT-PSPC pointed observations and the corresponding SRT count rates obtained from the RASS data. Both count rates are computed in the hard band (0.5-2.0 keV).

Fig. 17.— Comparison between the source counts measured within a  $5'$  radius circle from the emission peak and the ML source counts. The sample comprises EMSS pointlike objects observed in the RASS. Both were measured using the RASS data in the broad band (0.1-2.4 keV).

Fig. 18.— Correlation of the extension likelihood for a sample of bright RASS stars with the source count, using the results of the ML analysis. Both quantities were measured using the RASS data in the hard band (0.5-2.0 keV).







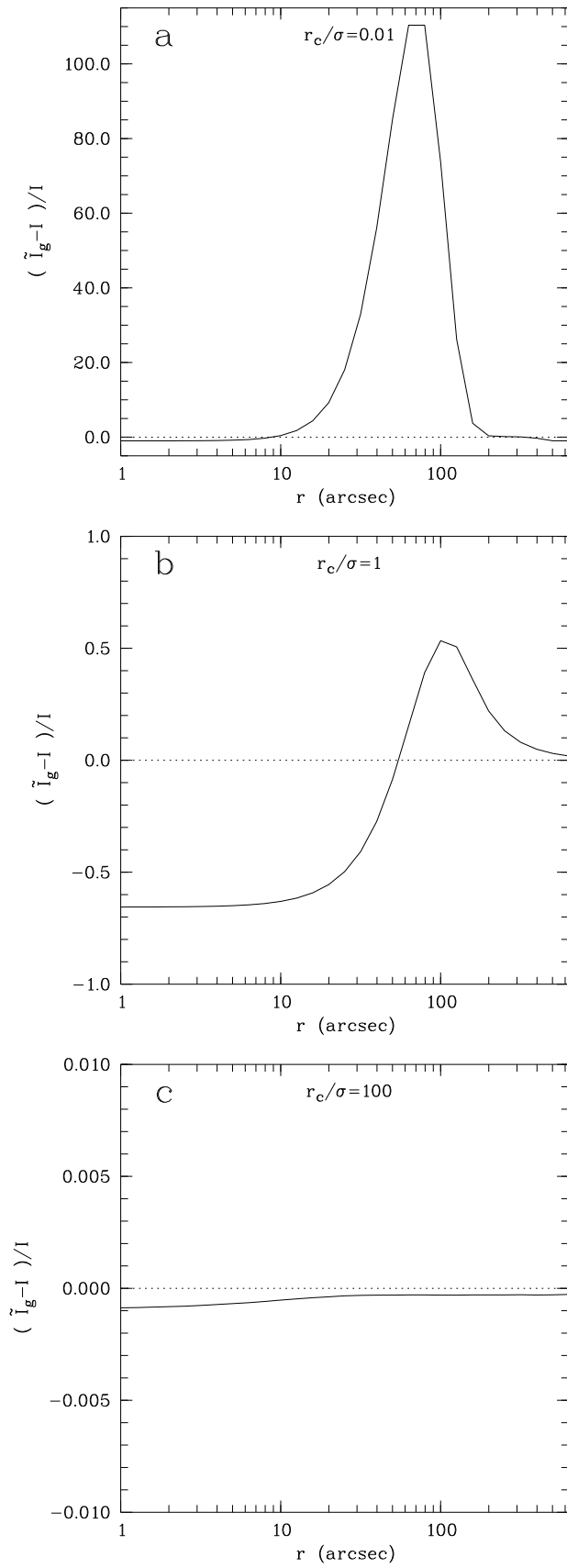


Fig. 3.—

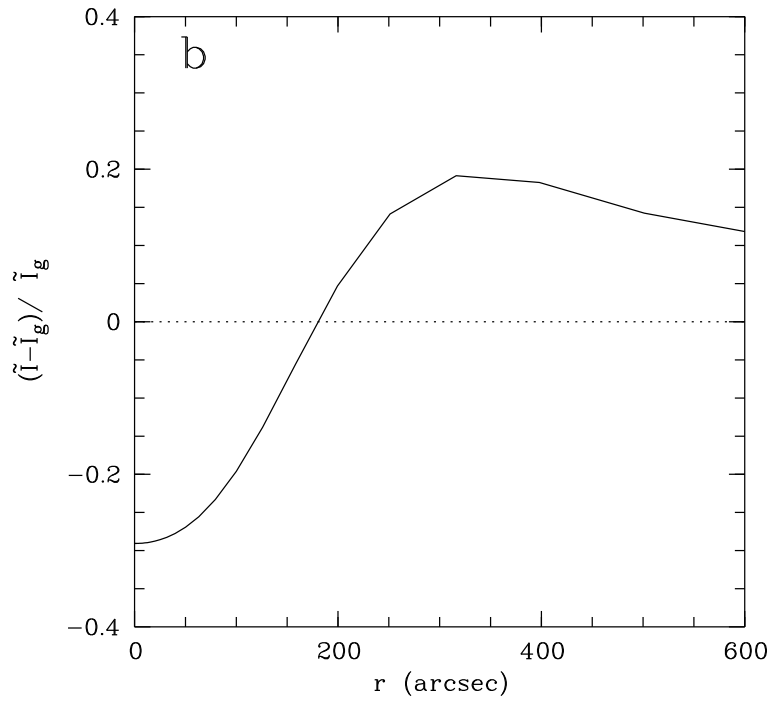
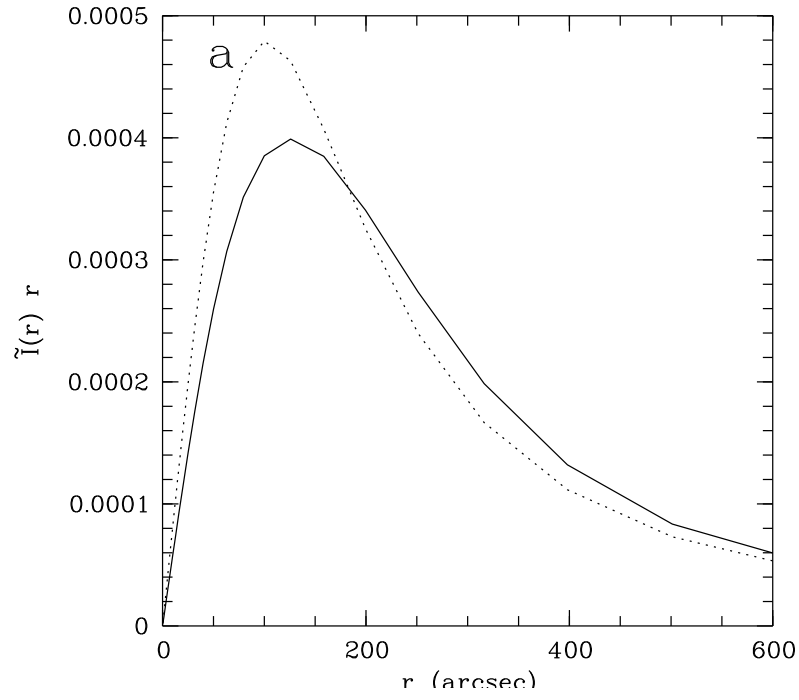


Fig. 4.—

